



ORIGINAL RESEARCH ARTICLE

Effect of Aging Condition on Microstructure, Mechanical Properties, and Shape Memory Behavior of Solution-Treated Fe-17Mn-5Si-5Cr-4Ni-0.2Ti-0.1C Shape Memory Alloy

Dohyung Kim, Eunyoung Choi, Hyunseok Cheon, and Wangryeol Kim

Submitted: 26 May 2023 / Revised: 21 July 2023 / Accepted: 24 July 2023 / Published online: 28 September 2023

In the present study, the effect of aging conditions on the microstructure, mechanical properties, and shape memory behavior of a solution-treated Fe-17Mn-5Si-5Cr-4Ni-0.2Ti-0.1C shape memory alloy was investigated. In addition, a revised mechanism for the precipitation-induced improvement of the shape memory effect (SME) is proposed. The effect of increasing the aging temperature from 500 to 900 °C was evaluated with a fixed time of 0.5 h, finding that the SME was initially improved upon increasing the temperature up to 600 °C, whereas further increasing the aging temperature exerted a detrimental effect on the SME. This was attributed to the change in the fractions of the ϵ and γ phases. The same increasing and constant trends were observed when the aging time was increased while maintaining the temperature constant at 600 °C. In this case, no change in the fractions of the ϵ and γ phases was detected. Instead, a change in the size and distribution of TiC precipitates might be the main reason for changes in properties. The presence of finer and densely distributed precipitates in the sample aged for 3.0 h could lead to a higher integrated pulling force, back stress, stacking faults, or ϵ phase cutting through the precipitates, resulting in a more effective back-transformation from ϵ to γ , compared with the sample aged for 6.0 h, which exhibits larger and sparsely distributed precipitates. Continuously decreased and increased 0.2% proof and tensile stress indicated an easier martensitic transformation in the early stage of deformation and precipitation hardening. However, according to the different trend in the SME and 0.2% proof stress, not only an easier martensitic transformation from γ to ϵ but also an integrated pulling force, which can be altered by tuning the size and distribution of precipitates, should be considered to achieve high SME induced by carbide precipitation.

Keywords electron backscatter diffraction, heat treatment, iron-based shape memory alloy, precipitation, recovery stress

1. Introduction

Shape memory alloys (SMAs) are novel functional metallic materials that can recover their original shape after deformation by external stimuli. This shape recovery behavior originates from a phase transformation between high-temperature austenite and low-temperature martensite. Depending on their recovery characteristics, the characteristics of SMAs can be roughly classified into pseudo- or super-elasticity (PE or SE) and shape memory effect (SME). The former recovers its shape immedi-

ately after removing the load. Because this deformation behavior resembles the elastic behavior and the recoverable strain is much greater than the original elastic limit, this behavior is called PE or SE. In contrast, the latter requires an external stimulus such as heat to recover.

Many types of SMAs have been developed to date, including Ni-Ti-based (Ref 1-3), Cu-Mn-Al-based (Ref 4-6), and Fe-based SMAs (Fe-SMAs) (Ref 7-9), among which Ni-Ti-based SMAs have been the subject of most studies and have found industrial application due to their excellent SME and PE behavior. However, the extremely high raw material cost and low machinability caused by their crystal structure limit their applicability. Conversely, despite their relatively low SME compared with that of Ni-Ti-based SMAs, Fe-Mn-Si-based Fe-SMAs have significantly lower production costs and higher machinability (Ref 7, 10), which render them suitable for large-scale industrial applications such as civil and structural engineering.

For instance, Lee et al. demonstrated that an Fe-17Mn-5Si-10Cr-4Ni-(V, C) alloy showed high recovery stress during shape recovery when subjected to precipitation hardening (Ref 11). Izadi et al. used the same type of alloy as a pre-stressing strengthening unit in concrete structures (Ref 12). In addition, Kajiwarra et al. reported that second-phase precipitation could also contribute to achieve good SME via the formation of

Dohyung Kim, Eunyoung Choi, and Wangryeol Kim, Dongnam division, Korea Institute of Industrial Technology, Yongsan 50623, Republic of Korea; and **Hyunseok Cheon**, Department of Material Science and Engineering, Pusan National University, Busan 46241, Republic of Korea; and Metallic Materials Division, Korea Institute of Materials Science, Changwon 51508, Republic of Korea. Contact e-mail: ryeol@kitech.re.kr.

stacking faults in the vicinity of the matrix–precipitate interface without any training process, i.e., repetitive deformation at ambient temperature and heating above A_f temperature, to form high stacking fault density (Ref 13).

Fe-SMAs could also find application as a bias component of linear actuators. Unlike civil engineering applications, which focus on recovery stress rather than SME, linear actuator applications require both high recovery stress and SME. To achieve high recovery stress and an appropriate SME, high yield strength is essential (Ref 14). In this regard, Kim et al. reported that a hot-rolled Fe-17Mn-5Si-5Cr-4Ni-0.2Ti-0.1C alloy exhibited a high SME of 3.21% under a pre-strain of 5.26% and a high 0.2% proof yield stress of 443 MPa (Ref 15). They also investigated the effect of the heat treatment temperature on the shape memory properties, finding that the SME increased slightly upon increasing the heat treatment temperature up to 600 °C and then dropped sharply when heating above 800 °C. Although the SME was increased at relatively low heat treatment temperature, the SME of an as-rolled sample not subjected to heat treatment was comparable to the highest SME achieved upon heat treatment. The authors claimed that the high SME in the as-rolled sample might be ascribed to the training effect and the formation of TiC precipitates during the repeated hot-rolling process. Therefore, the contribution of the TiC precipitation could not be independently confirmed. In this context, a solution-treated Fe-17Mn-5Si-5Cr-4Ni-0.2Ti-0.1C alloy was prepared to investigate the effect of the aging conditions on the microstructure and shape memory properties. Although Stanford et al. previously reported the effect of heat treatment on the shape memory properties of a TiC-containing SMA, further work is still required to unveil the property–microstructure relationship (Ref 16).

In this study, solution-treated Fe-SMA samples with a composition of Fe-17Mn-5Si-5Cr-4Ni-0.2Ti-0.1C (hereinafter referred to as Fe-SMA unless otherwise stated) were aged at different temperatures and times to investigate the microstructural changes in terms of phase fraction and precipitation behavior as a function of the heat treatment conditions. The findings revealed the influence of each factor on the SME and mechanical properties. In addition, a revised back-stress mechanism generated by precipitates is proposed.

2. Experimental Details

The chemical composition of Fe-SMA provided by manufacturer (Hankook Vacuum Metallurgy Co., Ltd., Republic of Korea) is listed in Table 1. First, Fe-SMA was melted in an induction melting pot under vacuum, and approximately 50 kg of the melt was cast into a cylinder-shaped graphite crucible. After casting, the ingot was homogenized via heat treatment at 1250 °C for 6.0 h. After the homogenization treatment, the

Table 1 Chemical composition of Fe-SMA

Element	Fe	Mn	Si	Cr	Ni	Ti	C
Target, wt.%	Bal.	17.00	5.00	5.00	4.00	0.20	0.10
Actual, wt.%	Bal.	15.78	5.02	4.68	3.73	0.22	0.09

alloy ingot was forged to a thickness of 80 mm and step-wisely hot-rolled at 1000 °C until the thickness of the alloy became 5 mm (15 passes). The hot-rolled plates were solution-treated at 1100 °C for 2 h to obtain solution-treated samples (hereinafter referred to as AST). To characterize the effect of the aging temperature following solution treatment, the AST samples were heat-treated at 500, 600, 700, 800, and 900 °C for 30 min and air-cooled, affording aged samples 500HT, 600HT, 700HT, 800HT, and 900HT, respectively. To investigate the effect of the aging time, the AST samples were heat-treated at 500, 600, and 700 °C at various times (Table 2). To avoid oxidation, all the samples were wrapped in stainless steel foil during the heat treatment.

A differential scanning calorimetry (DSC, DSC 8000, PerkinElmer, US) analysis was conducted to confirm the phase transformation temperature in a temperature range of – 70 to 350 °C at a heating and cooling rate of 5 °C/min. The peak martensite transformation (M_p) and austenite transformation temperature (A_p) were determined by tangent method as presented in Fig. 1. Microstructural characterization of the Fe-SMA samples was performed using an optical microscope (Eclipse E200, Nikon, Japan) and a scanning electron microscope (SEM, JSM-7200F, JEOL Inc., JAPAN). Electron backscatter diffraction (EBSD, Nordlys nano, Oxford Instrument, UK) was used for further phase characterization with a step size of 0.4 μm . The samples for the microstructural analyses were mechanically ground using SiC papers and subsequently polished with alumina and 0.04 μm silica colloidal suspensions. The samples were color-etched using a 0.5% NH_4HF_2 and 1.2% $\text{K}_2\text{S}_2\text{O}_5$ (wt.) solution in distilled water.

Thermo-Calc software (Thermo-Calc AB, Stockholm, Sweden) was used to model the equilibrium phase diagram and associated phase fractions.

The shape recovery performance of Fe-SMA was investigated by conducting a strip bending and recovery test. To evaluate the SME via bending and heating tests, strips with dimensions of 100 (l) \times 3 (w) \times 0.8 (t) mm^3 were cut from blocks using electric discharge machining. For the bending test, the specimen was bent around a mold with a radius of 7.6 mm at 27 °C to be subjected to a bending pre-strain of \sim 5.26%. Details on the bending and recovery test procedures can be found in our previous study (Ref 17). A transmission electron microscopy (TEM) analysis was performed on the microstructures of the samples aged at 600 °C for 3.0 and 6.0 h using a Titan Themiz Z Thermofisher, USA microscope with an accelerated voltage of 200 kV. For the TEM analysis, thin foils were prepared using the focused ion beam (FIB) lift-out technique with a FIB, Helios G4 UC, Thermofisher, USA.

Table 2 Heat treatment condition to investigate the effect of aging time

Temperature, °C	Time, h	
500	2.0	4.0
	6.0	8.0
600	1.5	3.0
	4.5	6.0
700	1.0	2.0
	3.0	

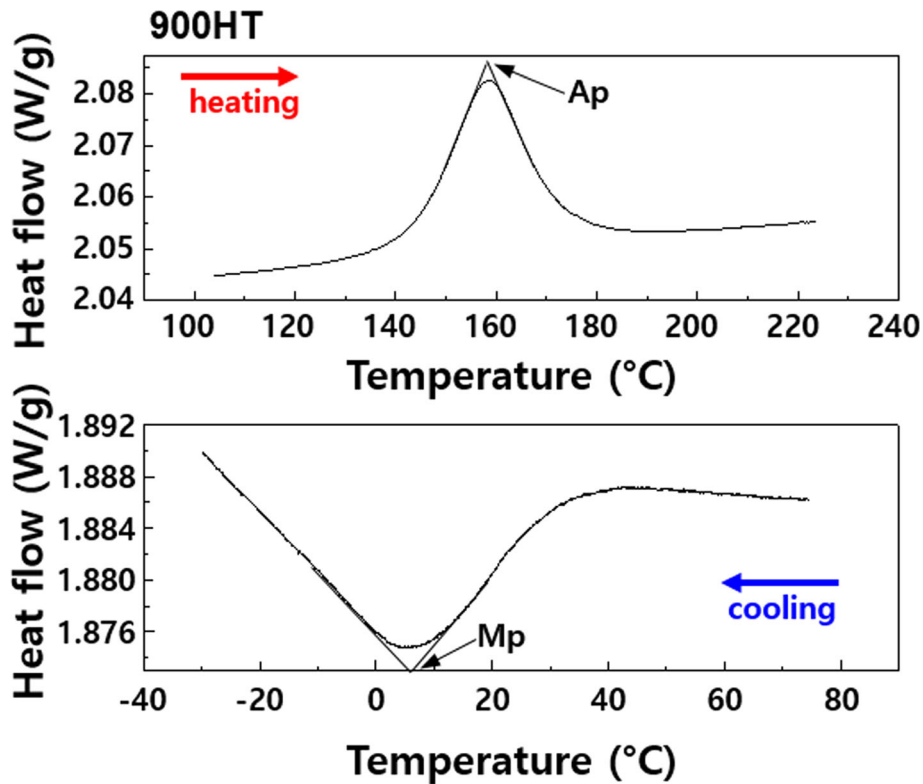


Fig. 1 Typical DSC curve and 'tangent method' to determine peak transformation temperatures

Tensile stress–strain curves of the samples were obtained according to the KS-B801 standard (Ref 18) using a flat-type dog-bone-shaped specimen with a gauge length of 13.2 mm, a width of 2 mm, and a thickness of 2 mm. Tensile tests were performed using a universal testing machine (RB 301 UNITECH-T, R&B Inc., Daejeon, Republic of Korea) with a constant loading rate of 1 mm/min. Strain gauges were attached to the specimens for elongation measurements.

3. Result and Discussion

3.1 Effect of Aging Temperature at a Fixed Time

Figure 2 shows representative optical microscope images of AST and samples aged at different temperatures for 0.5 h. For the optical microscopic analysis, the samples were etched using a color-etching solution, resulting in ϵ -martensite (hexagonal close-packed) and γ -austenite (face-centered cubic) phases appearing in white and brown colors, respectively. All samples showed large polygonal grains, implying that they were fully recrystallized and grown, and annealing twins (black dashed lines in Fig. 2). Annealing twins are commonly observed in solution-treated face-centered cubic metals and alloys having low stacking fault energy (Ref 19, 20). All sample showed extremely high fraction of ϵ phase with small fraction of γ phase. However, because the resolution of Fig. 2 is not enough to estimate the phase fractions of γ and ϵ , an EBSD phase analysis was conducted to quantify each phase fractions.

Figure 3 shows the EBSD phase maps of the solution-treated and aged samples. The quantitative values of the phase fractions are summarized in Table 3. Although the phase maps are not completely representative owing to the relatively high

magnification, Fig. 3 and Table 3 show clear increasing and decreasing trends in each phase. The AST sample showed an extremely high ϵ phase fraction of 96.91%, which was dramatically reduced upon heat treatment to 500°C and 600°C, whereas the γ phase fraction increased. However, upon further increasing the aging temperature, the change in the phase fractions followed the opposite trend.

First, the exceptionally high ϵ phase fraction in AST could be ascribed to thermal contraction during water quenching following solution treatment at 1100 °C. Stanford et al. reported the formation of stress-induced ϵ -martensite via not only isothermal deformation but also compressive contraction stress during cooling (Ref 21). This thermal contraction stress during cooling increases with the heat treatment temperature. In addition, the aged samples were cooled in air, whereas AST was subjected to water cooling, which could induce larger contraction stress due to a more rapid cooling rate, resulting in a more pronounced shear-induced phase transformation, i.e., γ -to- ϵ martensitic transformation. Meanwhile, the M_p temperature of AST (Table 4) was much higher than that of a similar alloy having a composition of Fe-17Mn-5Si-10Cr-(V, C) (−75°C), indicating that the alloy of the present study undergoes much more easily the martensitic transformation (Ref 22). In addition, the M_s (martensite transformation starting) temperature for ϵ -martensite (M_{ϵ_s}) of AST sample calculated by following empirical equation (Ref 23):

$$\begin{aligned}
 M_{\epsilon_s}(K) = & 576 - 489(\text{wt.\%C}) - 9.1(\text{wt.\%Mn}) - 17.6(\text{wt.\%Ni}) \\
 & - 9.2(\text{wt.\%Cr}) + 21.3(\text{wt.\%Al}) + 4.1(\text{wt.\%Si}) - 19.4(\text{wt.\%Mo}) \\
 & - 1(\text{wt.\%Co}) - 41.3(\text{wt.\%Cu}) - 50(\text{wt.\%Nb}) \\
 & - 86(\text{wt.\%Ti}) - 4(\text{wt.\%V}) - 13(\text{wt.\%W}),
 \end{aligned}
 \tag{Eq 1}$$

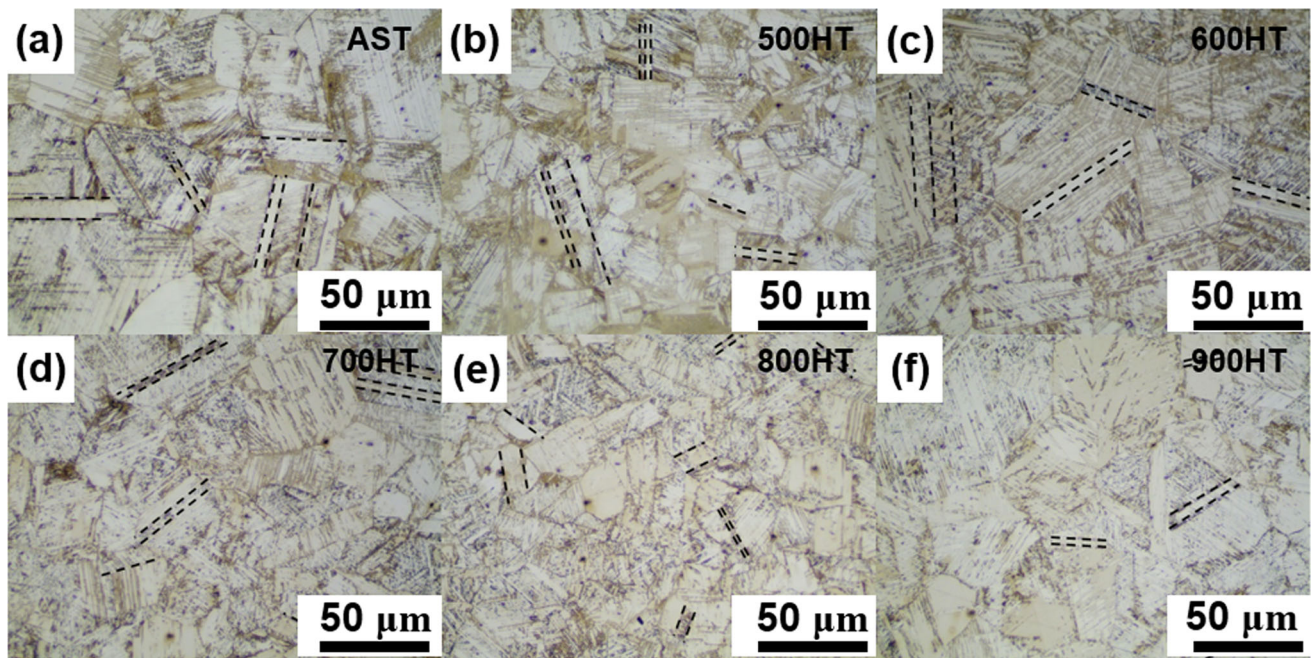


Fig. 2 Optical microscope images at low magnification ($\times 100$) of (a) solution-treated sample (AST) and samples aged at (b) 500 °C (500HT), (c) 600 °C (600HT), (d) 700 °C (700HT), (e) 800 °C (800HT), and (f) 900 °C (900HT). The black dashed lines indicate an annealing twin

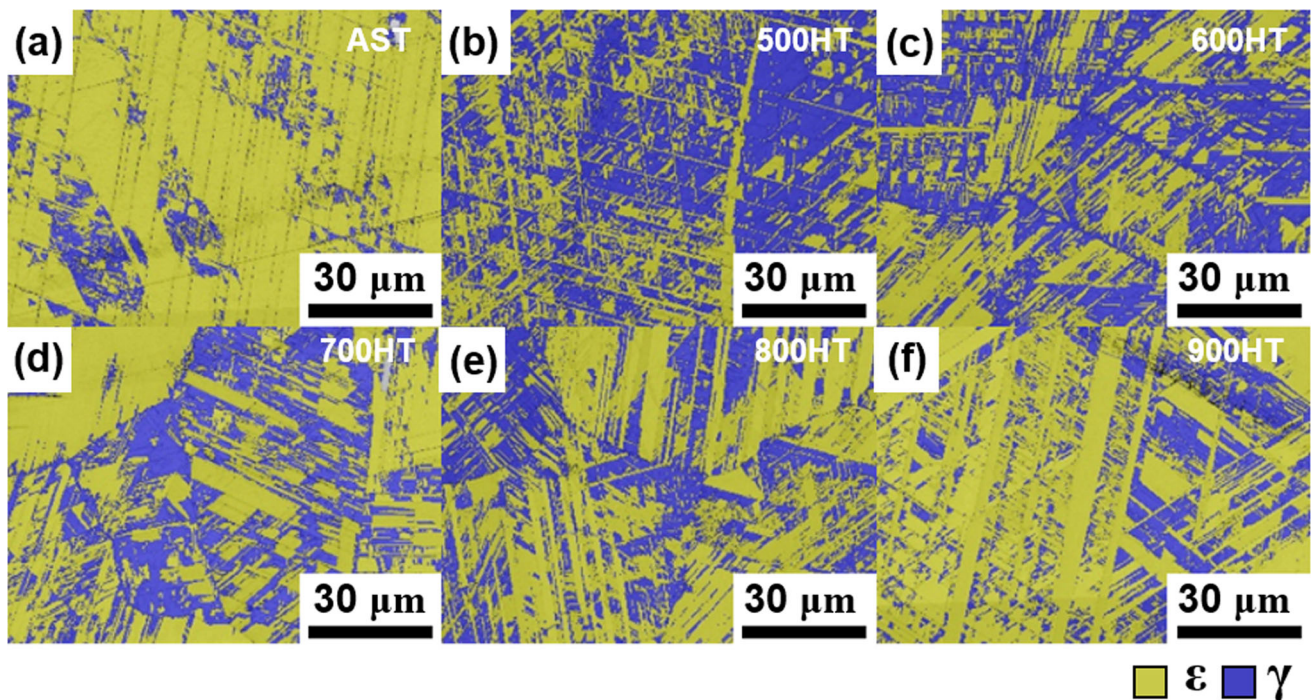


Fig. 3 EBSD phase maps of (a) solution-treated sample (AST) and (b)-(f) aged samples (500HT-900HT). The ϵ and γ phases are shown as yellow and blue colors, respectively (Color figure online)

was 13.2 °C. This higher Ms temperature can be explained in terms of its different chemical composition. The present alloy has lower Cr and C content, which is known to decrease the Ms temperature, resulting in reduced stability of the γ phase during cooling to room temperature (Ref 24, 25). As a result, the exceptionally high fraction of the ϵ phase in AST can be

attributed to the combined effect of large thermal contraction stress caused by the rapid cooling rate and reduced thermal stability. Even though the possible reasons for the high fraction of ϵ phase are listed above, both measured Mp and calculated Ms temperatures were lower than room temperature, making that the above reasons are not enough. However, because

Table 3 Phase fractions obtained via EBSD phase analysis

Sample		AST	500HT	600HT	700HT	800HT	900HT
Phase fraction, %	γ	9.94	51.86	53.78	32.68	30.21	21.72
	ε	86.91	47.48	45.32	66.24	68.59	77.09

Table 4 Phase transformation temperatures obtained via DSC analysis

Sample	AST	500HT	600HT	700HT	800HT	900HT
Mp, °C	− 11.65	− 20	− 10	− 11	3.61	7.37
Ap, °C	160.5	148.49	158.69	156.05	155.13	158.43

investigation of the origin of the extremely high ε fraction in AST sample is beyond the aim of this work, we remained it for future works.

Second, the respective increase and decrease in the fraction of γ and ε phases upon increasing the aging temperature to 600 °C can be explained by the thermal stability of each phase. As shown in Table 4, the Ap temperatures of all samples were much lower than the aging temperatures, implying that the reverse ε -to- γ phase transformation occurred during aging treatment. Conversely, the fraction of the ε phase increased again at higher aging temperatures. Kim et al. reported an increase in the ε phase fraction with increasing the heat treatment temperature, which stemmed from γ -austenite grain growth (Ref 15). Sahu et al. also reported that grain growth of the γ phase lowered its thermal stability (Ref 26, 27). However, in our case, the aging temperatures were much lower than the solution treatment temperature, which would hinder further grain growth. Instead, a larger thermal contraction stress during cooling compared with the case of lower aging temperatures might lead to the observed increase in the ε phase fraction.

Table 4 shows that the Mp temperature increased gradually with increasing the aging temperature above 700 °C, which might be attributed to a compositional change in the γ matrix as precipitation progressed. Fig. 4 shows magnified SEM images of AST and samples aged at increased temperatures for 0.5 h. No clear precipitates were observed in the images of AST, 500HT, and 600HT, suggesting that precipitation either did not occur at below 600 °C due to low diffusivity of the solute atoms or afforded too fine particles to be observed via SEM (Ref 28). Meanwhile, dispersed precipitates were observed when the aging temperature was higher than 600 °C. The thermodynamic simulation in Fig. 5 indicates that TiC, $M_{23}C_6$, and M_7C_3 carbides are potential precipitates. The M_7C_3 carbide can be disregarded because it only exists within a small temperature range of 720–760 °C and has an exceedingly low phase fraction of less than 0.2%. The $M_{23}C_6$ carbide, which is often $Cr_{23}C_6$, is known to be more likely to be seen on grain boundaries, according to publications concerning similar alloys (Ref 29). Additionally, the formation of $Cr_{23}C_6$ is greatly reduced by the presence of Ti (Ref 30). As a result, TiC precipitates may be present. Our previous study that described shape memory properties and microstructure of the same alloy also confirmed that the TiC can be precipitated in this alloy system (Ref 15). The precipitation became more pronounced

with increasing the aging temperature. According to the literature, carbide-forming elements such as Ti, V, or Nb do not solely form carbides like TiC, VC, or NbC, respectively. Cautaerts et al. found a relatively higher Cr content in carbides than in the matrix, as well as abundant Ti and C (Ref 31). Hence, it can be concluded that the increased precipitation of carbides consumed more Cr and C, resulting in increases in the Mp temperature and ε phase fraction in 800HT and 900HT.

Figure 6 shows the shape memory properties of the prepared Fe-SMA samples. The white, red, and green columns represent ε_{pse} , ε_{rec} , and ε_{tot} , respectively. Here, ε_{pre} , ε_{pse} , ε_{rec} , and ε_{tot} are pre-deformation strain, pseudo-elastic strain, shape recovery strain after heating and total recovery strain resulting from a summation of the ε_{pse} and ε_{rec} , respectively. The sample aged at 500 °C for 0.5 h showed lower ε_{pse} than AST. Upon further increasing the aging temperature, the ε_{pse} value increased slightly. Meanwhile, ε_{rec} and ε_{tot} initially increased and then decreased upon increasing the aging temperature, resembling the trend of the γ phase fraction. The variation of ε_{tot} highly depended on ε_{rec} because ε_{pse} was much lower than ε_{rec} , indicating that the SME is more pronounced than PE in this kind of Fe-SMAs. Therefore, this study mainly focused on the effect of the aging conditions on the SME.

The change in the SME can be explained by considering the change in the phase fractions. The increase in ε_{rec} for 500HT and 600HT was associated with an increase in the γ phase fraction. Because the origin of the SME is the reversible phase transformation between the stress-induced ε phase and the parent γ phase, the amount of transformable parent phase is decreased when there is a high fraction of the ε phase before deformation. Additionally, a substantial quantity of pre-existing ε phase is anticipated to form α' phase (body-centered cubic or tetragonal) during collision with stress-induced martensite, resulting in an irrecoverable strain component. In fact, the change in the SME and the γ phase fraction followed the same trend. This can also explain the decrease in ε_{rec} at higher aging temperatures resulting in a higher fraction of the ε phase. Therefore, the initial increase in the SME at low aging temperatures of 500°C and 600°C was highly affected by the increase in the γ phase fraction.

Although the phase fraction of 800HT was just 2.47% lower than that of 700HT, the ε_{rec} of 800HT decreased to 2.33% from the value of 2.87% for 700HT. This decrease in ε_{rec} was nearly identical to that observed for 600HT and 700HT. Considering

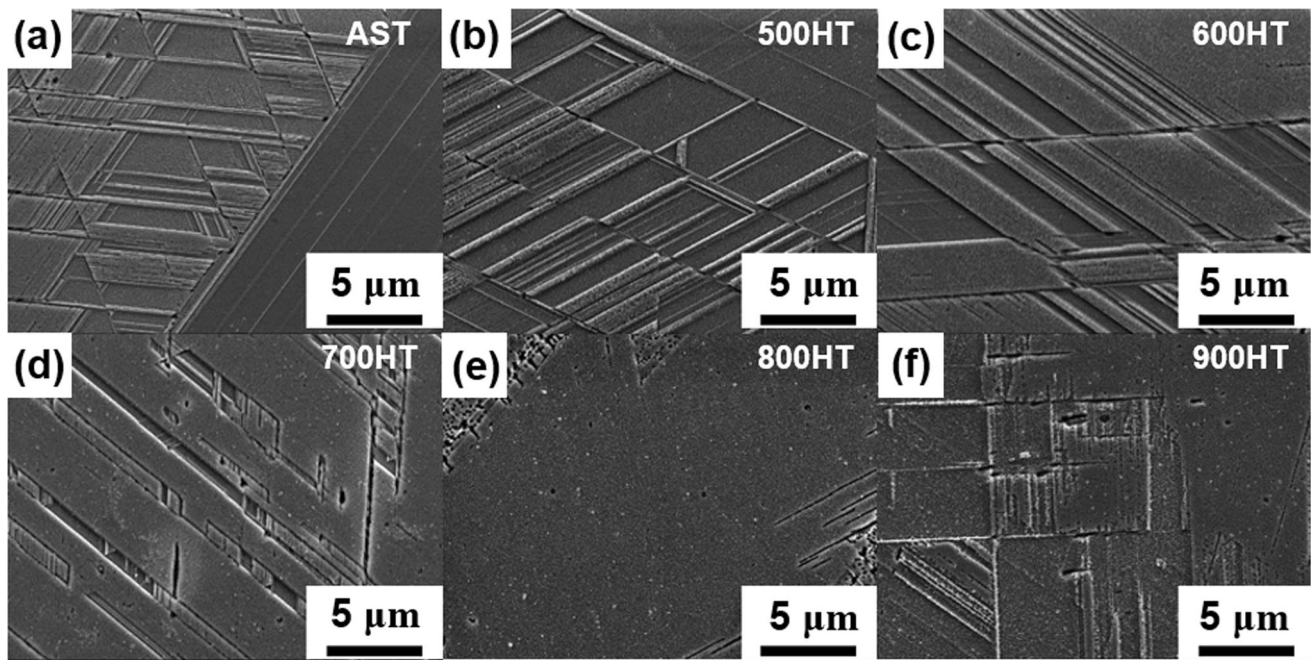


Fig. 4 SEM images of a solution-treated sample (AST) and samples aged at different temperatures for 0.5 h. (a) AST, (b) 500HT, (c) 600HT, (d) 700HT, (e) 800HT, and (f) 900HT

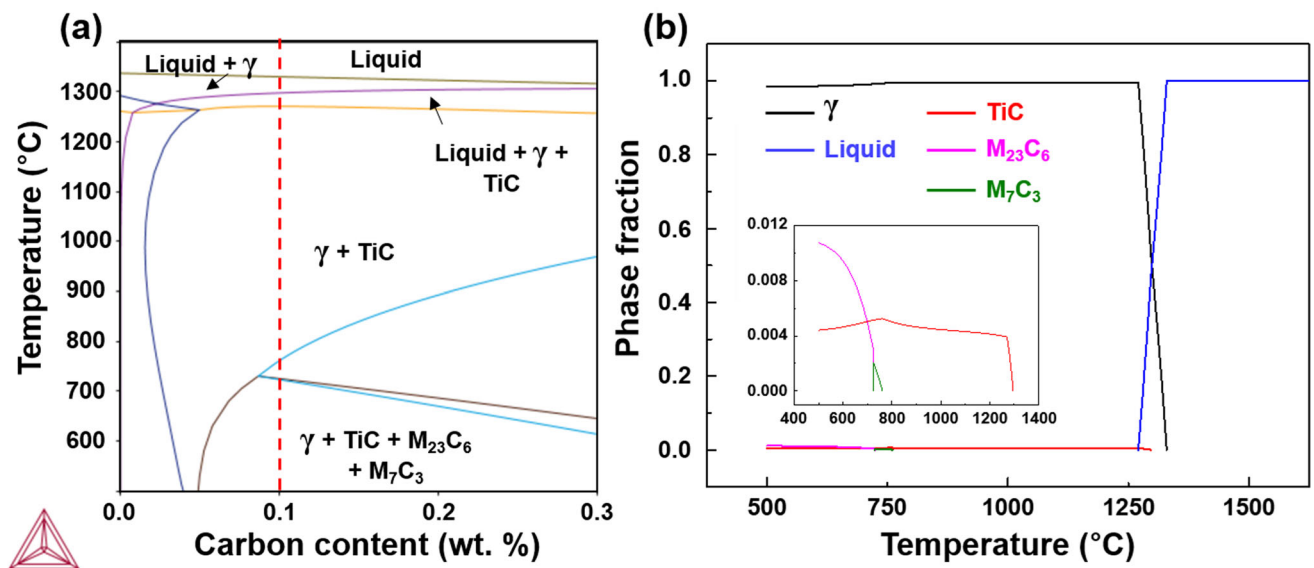


Fig. 5 (a) Equilibrium phase diagram for Fe-17Mn-5Si-5Cr-4Ni-0.2Ti-xC (wt. %) (b) Equilibrium phase fraction of Fe-17Mn-5Si-5Cr-4Ni-0.2Ti-0.1C as a function of temperature with an inset showing the phase fraction of carbides. Both were calculated by Thermo-calc software

the large difference in the γ phase fraction between 600HT and 700HT, there should be another factor affecting the SME. As shown in Table 4, the M_p temperature began to increase at an aging temperature of 800°C. Since the M_p temperature is highly affected by the chemical composition, a pronounced compositional change can be expected in this case. As aforementioned, the more pronounced precipitation in 800HT

compared with 700HT might consume more Cr, resulting in depletion of the Cr content in γ matrix. According to Guerrero et al., the addition of Cr has a positive effect on the SME because it decreases the volume change during the transformation between γ and ϵ phases (Ref 25). In this case, the decrease in Cr content in the γ matrix could reduce the reversibility of the transformation between γ and ϵ phases.

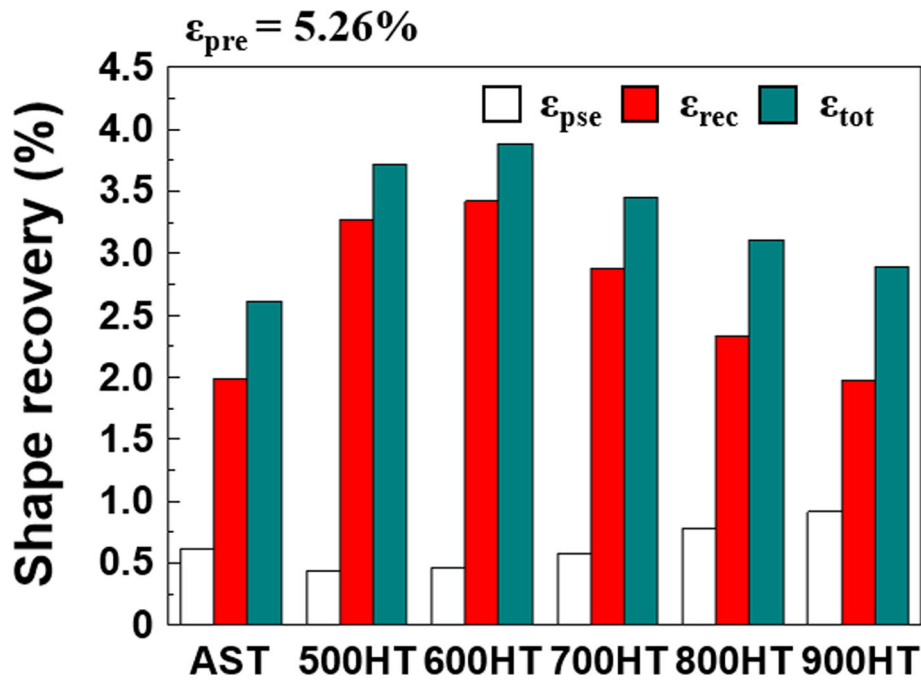


Fig. 6 Shape memory properties of a series of Fe-based shape memory alloys (AST: solution-treated sample; 500HT, 600HT, 700HT, 800HT, and 900HT: samples aged at different temperatures)

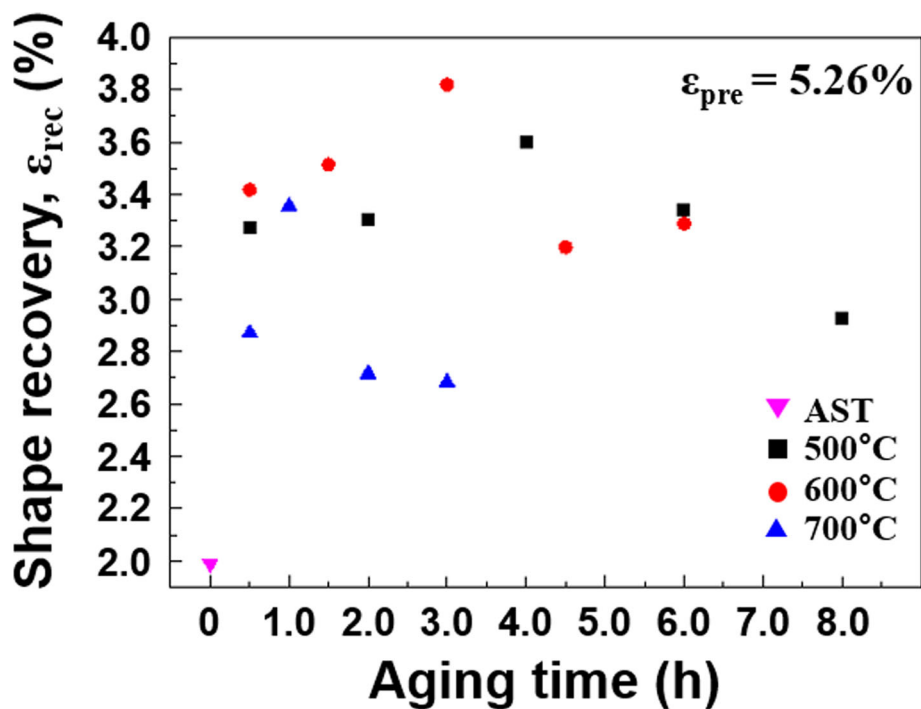


Fig. 7 SME (ϵ_{rec}) of the Fe-SMA samples aged at three aging temperatures for various times

Although more pronounced precipitation was confirmed at higher aging temperatures, the effect of precipitation could not be independently evaluated because it was accompanied by a large change in the phase fraction and chemical composition. To gain more insight into the effect of precipitation, solution-treated samples were aged at the same temperature for various times.

4. Effect of Aging Time at the Same Temperature

Figure 7 shows SME (ϵ_{rec}) of the AST and samples aged at three different temperatures for various times. As the aging time increased, the SME initially increased up to a peak value and then decreased for all aging temperatures. The highest and lowest peak values were obtained by aging at 600 °C and

700 °C, respectively. The SME change trend at the times corresponding to peak values was the same with that of the samples aged for a fixed time (0.5 h), which might be due to the difference in γ and ϵ phase fractions. Leaving the SME change as a function of the aging temperature aside, the SME trend of initially increasing and then decreasing indicates the occurrence of important microstructural changes during the aging treatment for different times. To reveal the effect of the aging time, a set of samples aged at 600 °C for four different times, i.e., 1.5, 3.0, 4.5, and 6.0 h, were investigated.

The EBSD phase maps of the samples aged at 600 °C for different times are presented in Fig. 8, and the corresponding phase fractions are summarized in Table 5. Although the γ phase fraction decreased slightly and that of ϵ increased as the aging time became longer, these changes were less pronounced compared with those observed when varying the aging temperature. The M_p and A_p temperatures presented in Table 6 also show no significant differences as a function of the aging time, indicating that compositional changes were limited during aging.

High-magnification SEM images of the samples aged at 600 °C for various lengths of time are shown in Fig. 9.

Table 5 Phase fraction of samples aged at 600 °C for different times obtained via EBSD phase analysis

Aging time, h		1.5	3.0	4.5	6.0
Phase fraction, %	γ	50.86	47.02	45.26	44.78
	ϵ	48.37	51.76	53.80	54.21

Table 6 Phase transformation temperatures of samples aged at 600 °C for different times obtained via DSC analysis

Aging time, h	1.5	3.0	4.5	6.0
M_p , °C	− 16.44	− 9.43	− 12.42	− 6.73
A_p , °C	158.69	155.11	152.99	151.37

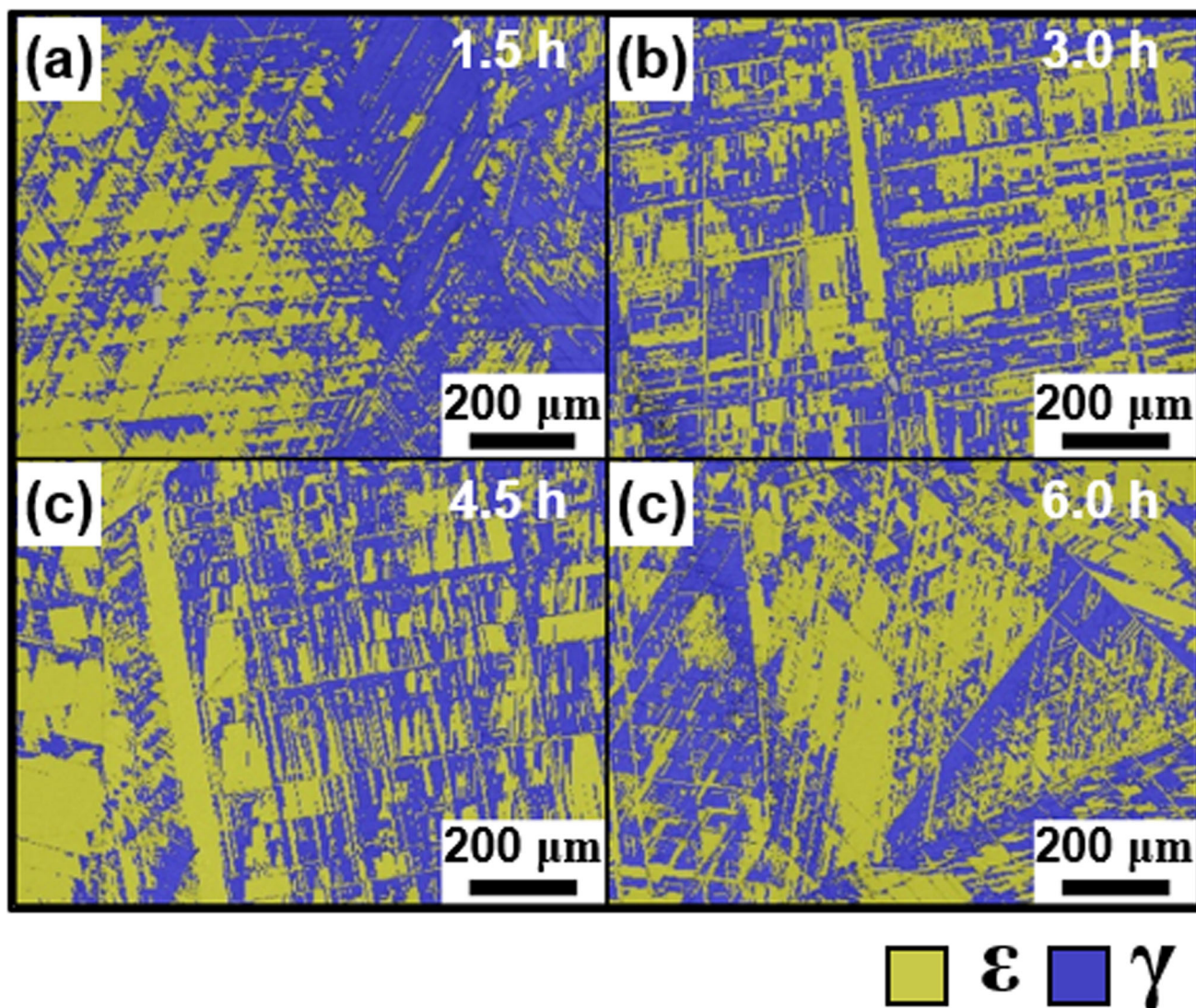


Fig. 8 EBSD phase maps of samples aged at 600 °C for (a) 1.5 h, (b) 3.0 h, (c) 4.5 h, and (d) 6.0 h

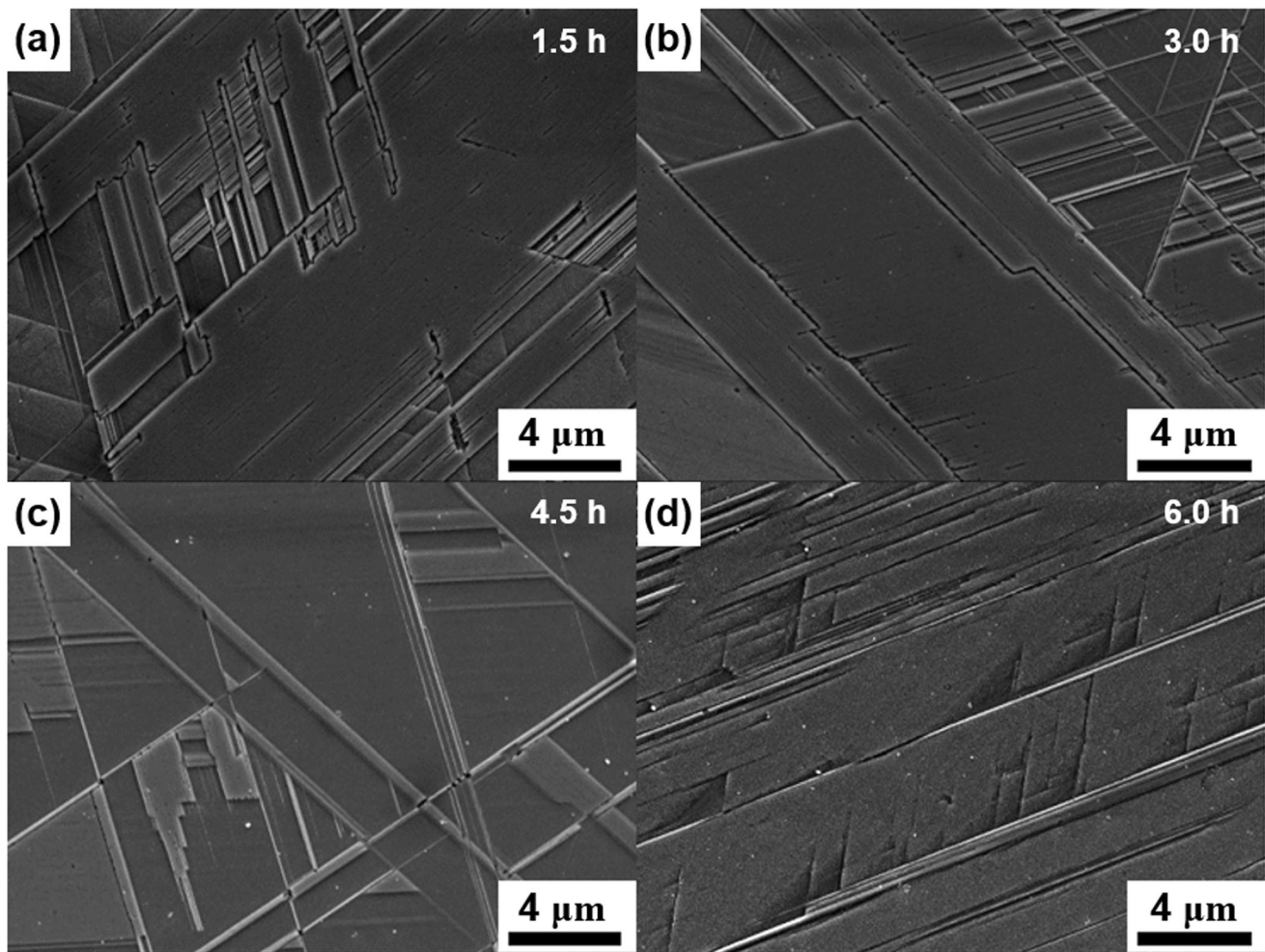


Fig. 9 High-magnification SEM images of samples aged at 600 °C for (a) 1.5 h, (b) 3.0 h, (c) 4.5 h, and (d) 6.0 h

Although small white spots that may represent TiC precipitates resembling Fig. 3 can be detected in Fig. 8 (c) and (d), precipitates were hardly discernible in Fig. 8. However, Fig. 10 (b) and (d) shows that tensile strength gradually increased with aging time, indicating that more precipitation strengthening occurred throughout aging treatment. In addition, more conspicuous white dots in Fig. 9(d) indicate the growth of precipitates. This might be ascribed to a diffusion process. Upon increasing the aging time, more carbide-forming elements diffuse, promoting the growth of precipitates. The growth of precipitates as the aging time increases has been reported for many types of alloys (Ref 32, 33).

5. Mechanical Properties

Figure 10 shows the mechanical properties of aged Fe-SMA samples, and Table 7 summarizes the quantitative values. The AST sample exhibited the highest 0.2% proof stress and the lowest fracture elongation and tensile stress. The poor mechanical property of the AST sample could be attributed to the extremely high fraction of the ϵ phase having only a few slip systems. Furthermore, a low γ phase fraction led to a decrease in the potential transformation-induced plasticity, resulting in poor strength, and fracture elongation. When the Fe-SMA

samples were aged at elevated temperatures for a fixed time, the 0.2% proof stress decreased with increasing the tensile stress by heating at 700 °C, as shown in Fig. 10 (a, c). Because the onset of the transition from the elastic to plastic regime has been considered as the onset of martensitic transformation for this type of alloys with low stacking fault energy, the decrease in the 0.2% proof stress indicates that stress-induced martensitic transformation can occur at lower stress values, i.e., the phase transformation from γ to ϵ proceeds more easily (14).

Furthermore, the increase in tensile stress can be attributed to precipitation hardening. These can support the fact that precipitation hardening with much finer precipitates may occur even at relatively lower temperature, 500 and 600 °C even though the precipitates are not observed in Fig. 4 (b) and (c), and it also explains the slight increase of ϵ_{rec} in 600HT compared to 500HT. The decrease and increase in 0.2% proof and tensile stress in 600HT compared to 500HT are evidence of more pronounced precipitation behavior.

When the aging temperature was 800 °C, the 0.2% proof stress suddenly increased most likely due to the difference in the size of the precipitates. Stacking faults cut through the precipitates when the size of the precipitates is extremely fine (Ref 34). At aging temperatures below 800 °C, the precipitates might not be sufficiently large to prevent the movement of dislocations, indicating that the Orowan by-passing mechanism does not operate effectively in the early stage of deformation.

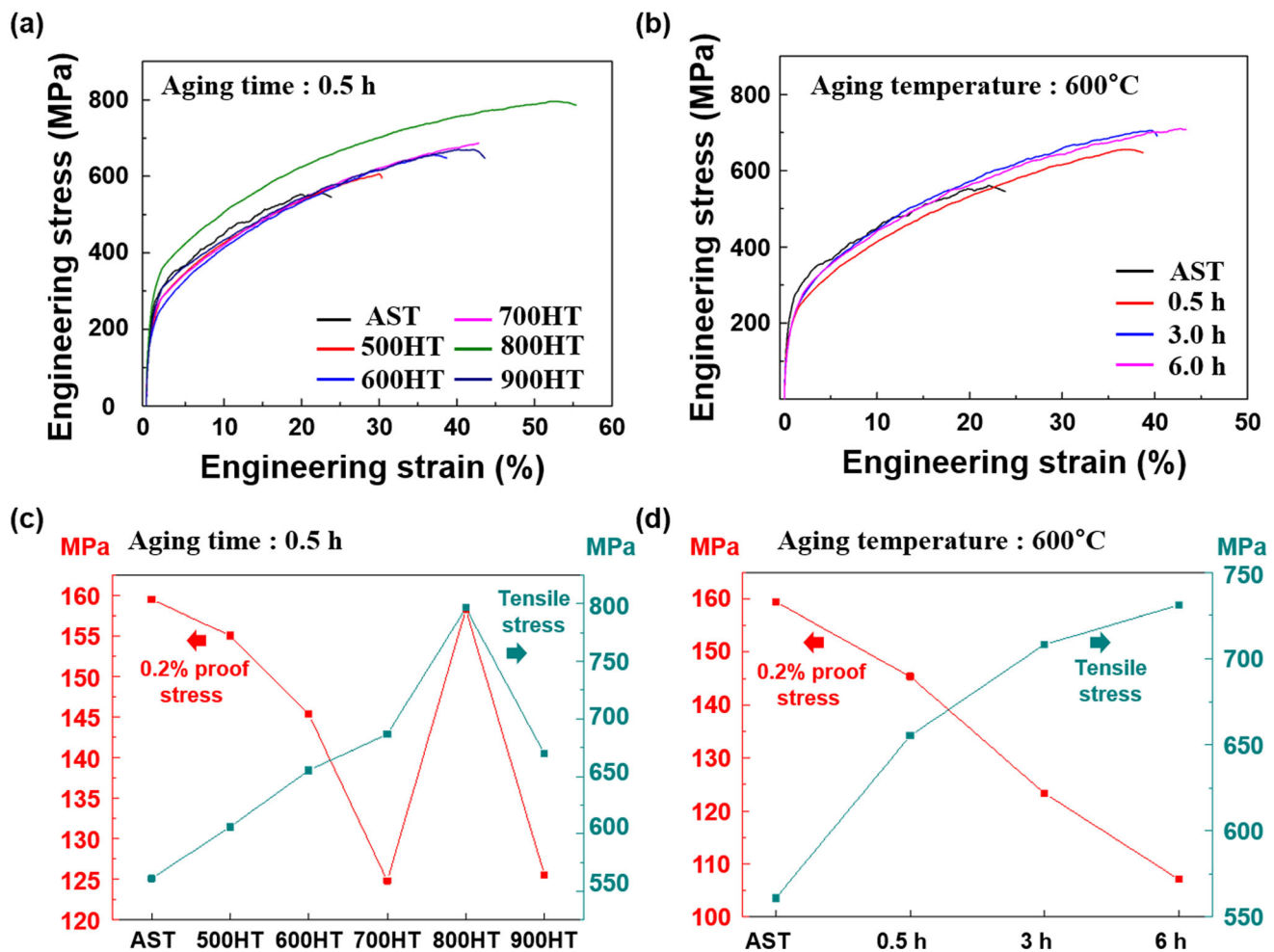


Fig. 10 (a), (b) Typical engineering stress–strain curves and (c), (d) changes in 0.2% proof stress and tensile stress of a solution-treated sample (AST) and Fe-based shape memory alloy samples (500HT–900HT) (a), (c) aged at various temperatures for 0.5 h and (b) aged at 600 °C for various times, respectively

Table 7 Mechanical properties of aged Fe-SMA samples

Heat treatment condition	0.2% proof yield strength, MPa	Tensile strength, MPa
No aging (AST)	159	561
500 °C, 0.5 h (500HT)	155	606
600 °C	145	655
0.5 h (600HT)	125	708
3.0 h	107	731
6.0 h		
700 °C (700HT)	125	686
800 °C (800HT)	158	796
900 °C (900HT)	125	669

As a result, the effect of the easy martensitic transformation is more predominant than the strengthening effect, resulting in a lowering of the 0.2% proof stress. In contrast, if precipitates formed during aging at 800 °C for 0.5 h are sufficiently large to inhibit the cutting through of stacking faults, the movement of partial dislocations could be effectively disturbed by the Orowan by-passing mechanism in the early stage of deformation. This increase in the 0.2% proof stress for 800HT could be also related to its lower SME compared with that of 700HT,

although both samples have similar ϵ and γ phases fractions. As discussed above, a high 0.2% proof stress is indicative of a difficult martensite transformation. The significantly increased fracture elongation of 800HT, meantime, remained unclear. This exceptionality was not determined to be an experimental error thanks to the repeated test. The deformation process and interactions of the dislocation with carbides or grain boundaries are responsible for the change in strength and ductility. However, further investigation of such behavior should be

required using more in-depth analysis. Therefore, a further study will be conducted to learn more about the uncommon behavior. However Upon further increasing the aging temperature, both 0.2% proof and tensile stress for 900HT decreased again. This could be due to the TiC precipitates formed during aging at 900 °C for 0.5 h being large enough to lose coherency with the matrix, resulting in a less effective interruption of the movement of dislocations despite the highest ϵ phase fraction among the heat-treated samples (Ref 35). Because the 0.2% proof stress is strongly related to the onset of phase transformation from γ to ϵ phase, the low 0.2 % proof stress of 900HT, in spite of the highest ϵ phase fraction, can be attributed to the weakened γ phase.

Figure 10 (b) and (d) show the mechanical properties of the Fe-SMA samples aged at 600 °C for various times. In this case, the 0.2% proof and tensile stress were monotonically decreased and increased, respectively, similar to Fig. 10 (a) and (c), which means that the martensitic transformation occurs more easily in the early stage of deformation and precipitation hardening, respectively. However, although the 0.2% proof stress was monotonically decreased when the aging temperature was increased up to 700 °C for 0.5 h and the aging time was prolonged up to 6.0 h at 600 °C, the SME showed peak values in both cases. This indicates that the size and distribution of precipitates do not affect equally the SME and the mechanical properties. Furthermore, this is inconsistent with the general idea that an easier martensitic transformation, i.e., lower proof stress, induced by precipitation can enhance the SME. Especially, because the samples aged at the same temperature for different times have similar phase composition, there should be another factor affecting the SME.

6. Discussion

According to Kajiwara et al., NbC precipitates can be not only potential nucleation sites for stress-induced martensite but also obstacles for martensite growth, causing back stress acting on the approaching martensite tip due to an elastic field generated by coherent lattice misfit (Ref 13). In addition, the back stress promotes reverse motion of Shockley partial dislocations during heating, i.e., reverse phase transformation from ϵ to γ , resulting in a remarkable improvement of SME without training. Lai et al. also reported an improved SME induced by the precipitation of VC (Ref 34). However, they claimed that single-variant and extremely thin martensite plates were responsible for the improved SME rather than back stress because the precipitates were cut through by Shockley partial dislocations. In the present study, both samples aged at 600 °C for 3.0 and 6.0 h had extremely thin ϵ plates with a few nm as presented in Fig. 10. Hence, the thickness of the ϵ plates is not sufficient to explain the difference in SME. Otherwise, the lower density of stacking faults in the sample aged at 600 °C for 6.0 h could be a possible reason for the lower SME due to the fact that the high density of pre-existed stacking faults promotes γ to ϵ phase transformation. However, the lowest 0.2 % proof stress implies taking place the phase transformation at a low-stress level, that is, easy transformation. Consequently, it could be concluded that the relatively lower staking fault density was also not a critical factor for the lower SME.

On the other hand, although it was difficult to directly confirm the presence of TiC precipitates in the former, the

results of mechanical testing indirectly indicate precipitation behavior and it can be expected that the more fine precipitates were distributed. Assuming that the back stress was still effective despite the Shockley partial dislocations or ϵ plates cutting through the precipitate, the back stress generated by more densely distributed precipitates could act more effectively on the stress-induced ϵ phase compared with that generated by less dense precipitates. In the sample aged at 600 °C for 3.0 h, coherent TiC precipitates of a few nm size are visible in Fig. 11 and are being cut through by the ϵ phase. Despite the heavily faulted structure in Fig. 12 (a) results in poor image quality, the accompanying Fast Fourier Transformation image in Fig. 12 (b) shows the presence of coherent precipitates. The inverse fast Fourier transformation (IFFT) image in Fig. 12 (c) using the spots corresponding to precipitates also shows the presence of precipitates. In this case, the concept of back stress proposed by Kajiwara et al. could be revised into a pulling stress acting on the Shockley partial dislocation or ϵ plates cutting through the precipitates rather than a pushing stress against the approaching martensite tip. The revised mechanism for the improved SME is schematically illustrated in Fig. 13.

During stage I, where more TiC with nm size precipitates as a function of the aging time, more back stress can be generated by densely distributed precipitates. As a consequence, the integrated back stress generated by precipitates on the same ϵ plates cutting through them can more effectively pull the ϵ plate tip, improving the SME. Meanwhile, the precipitates agglomerate during stage II, resulting in sparsely distributed coarse precipitates. Since the less densely distributed TiC particles limit the number of sites for the generation of back stress, the integrated pulling force acting on the ϵ plate tip is weakened. It is worth emphasizing at this point the importance of the back stress acting on the stacking faults or ϵ phases that cut through the precipitates. Although larger precipitates can facilitate martensitic phase transformation by lowering the 0.2% proof stress, the reduced back stress due to a greater mean distance between precipitates could not effectively induce the back-transformation from ϵ to γ .

7. Conclusions

In this study, the effect of the aging conditions on the microstructure, mechanical properties, and shape memory behavior of a solution-treated Fe-17Mn-5Si-5Cr-5Ni-0.2Ti-0.1C alloy was investigated. The findings revealed that the initial ϵ phase fraction and the TiC precipitation behavior resulting from the aging treatment highly affected both the shape memory and the mechanical properties. The main results can be summarized as follows:

- 1) Solution-treated Fe-SMA showed the poorest shape memory and mechanical properties due to an extremely high ϵ phase fraction (86.91 %).
- 2) As the aging temperature gradually increased up to 600 °C at a fixed time (0.5 h), the SME increased. The improvement of the SME might be due to decreased pre-existed ϵ phase fraction (45.32 %). However, further increasing the aging temperature caused a decrease in the SME due to an increase in the ϵ phase fraction up to 77.09 %. The changing trend of SME was the same as that of the phase fraction.

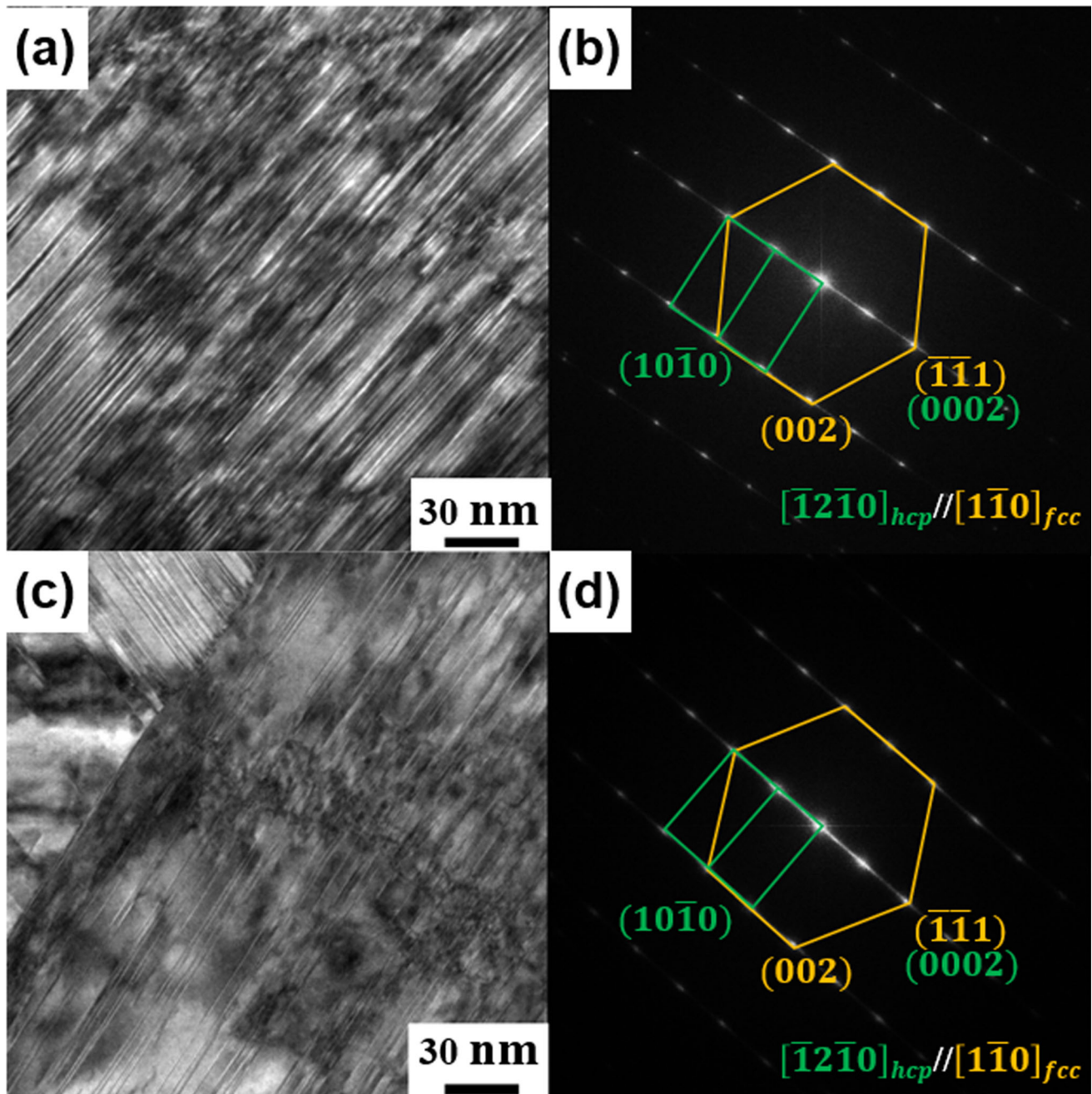


Fig. 11 TEM bright-field images and corresponding selected area diffraction patterns of the samples aged at 600 °C for 3 h and 6 h. (a), (b) 3 h, and (c), (d) 6 h

3) Upon gradually increasing the aging time up to 3.0 h at a fixed temperature (600 °C), the SME increased, whereas it decreased with further prolonging the aging time. This behavior can be ascribed to changes in TiC precipitates behavior. SEM analysis revealed growth of the precipitates in the sample aged for 6.0 h, but there was no evidence of precipitation in the sample aged for 3.0 h. However, the decreased 0.2 % proof stress and increased tensile strength proved the occurrence of precipitation, which is expected to have much finer particles during the aging for 3.0 h. The finer precipitates could apply higher integrated pulling force on stacking faults

and ϵ phase cutting through the precipitates than larger and sparser precipitates.

4) Except for 800HT and 900HT, the 0.2% proof stress and tensile stress monotonically decreased and increased, respectively, upon increasing the aging temperature at a fixed time and upon increasing the aging time at a fixed temperature. The increasing behavior in the tensile stress stems from precipitation hardening. In contrast, the continuous decrease in the 0.2% proof yield stress is indicative of an easier martensitic phase transformation, and the SME showed peak values during the increase in aging temperature and time. This indicates that there was

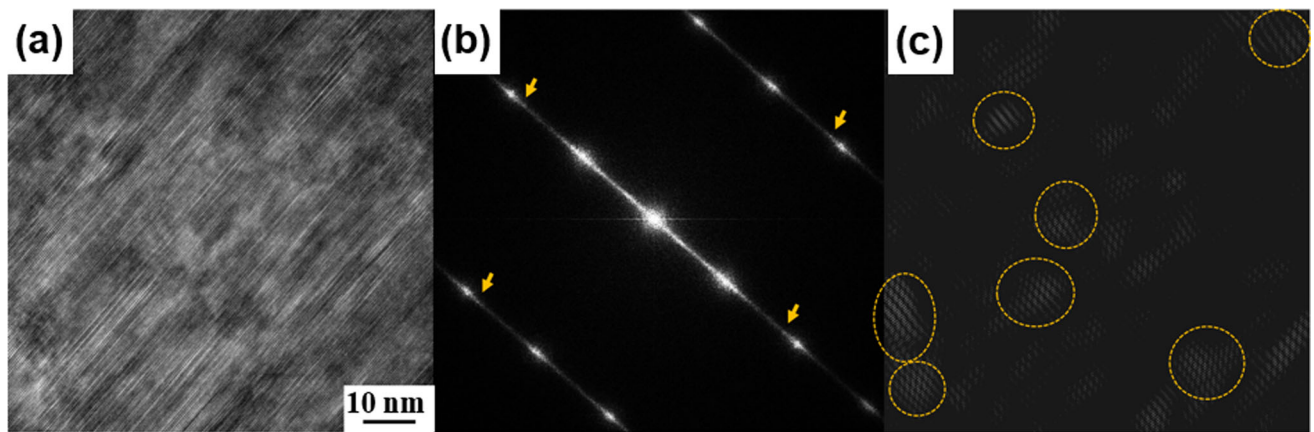


Fig. 12 (a) High-magnification TEM bright-field image of the sample aged at 600 °C for 3.0 h, (b) the corresponding FFT image, and (c) IFFT using diffraction spots indicated by yellow arrows in (b) (Color figure online)

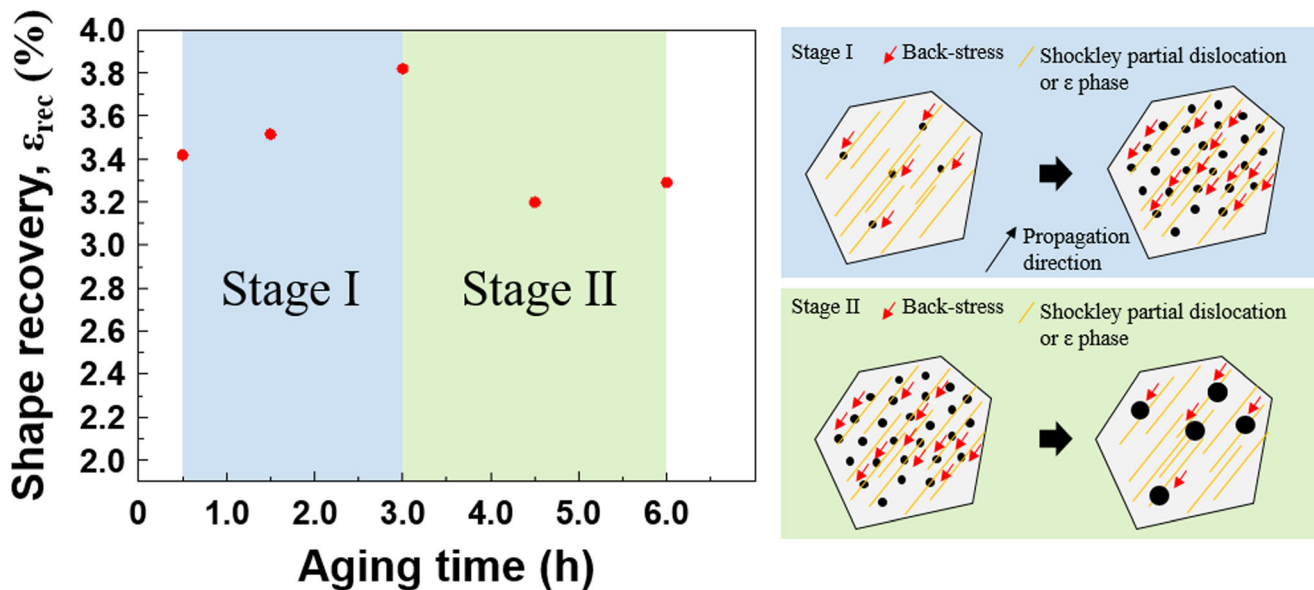


Fig. 13 Illustration of the revised mechanism for the improved shape memory effect

a critical precipitate size to generate the maximum back stress resulting in maximum SME even though the onset of martensitic transformation was continuously lowered.

- Therefore, to obtain high SME in this kind of precipitation hardenable Fe-SMAs, finding the critical precipitate size that affords the maximum SME is as important as lowering the onset stress for martensitic phase transformation and the initial ϵ phase fraction.

Although a revised mechanism was proposed and the effect of aging conditions on shape memory and mechanical properties was investigated in this study, direct observations of change in the size of the precipitates over time and interactions between propagating martensite tip and precipitates are required to demonstrate the proposed mechanism and quantitative relationship between precipitation behavior and material

properties. The current authors will conduct the above investigations in more detail in the near future.

Acknowledgments

This research was financially supported by the Ministry of Trade, Industry and Energy (MOTIE), Korea Institute for Advancement of Technology (KIAT), through the International Cooperative R&D program (Project No. P0019307).

Author Contributions

DK helped in conceptualization, methodology, visualization, data curation, and writing—original draft. EC and HC investigated microstructure and phase transformation characteristics using electron backscatter diffraction and differential scanning calorimetry. WK helped in funding acquisition, supervision, and writing—review and editing.

Data availability

The raw/processed data required to reproduce these findings cannot be shared at this time as the data also form part of an ongoing study.

Conflict of interest

The authors declare no conflict of interest and have no known competing financial interests or personal relationships that could have appeared to influence the work reported in this paper.

References

1. F.E. Wang, W.J. Buehler, and S.J. Pickart, Crystal Structure and a Unique “Martensitic” Transition of TiNi, *J. Appl. Phys.*, 1965, **36**(10), p 3232–3239. <https://doi.org/10.1063/1.1702955>
2. H. Yu and M.L. Young, Effect of Temperature on High Strain Rate Deformation of Austenitic Shape Memory Alloys by Phenomenological Modeling, *J. Alloys Compd.*, 2019, **797**, p 194–204. <https://doi.org/10.1016/j.jallcom.2019.05.041>
3. H. Yu, Y. Qiu, and M.L. Young, Influence of Ni₄Ti₃ Precipitate on Pseudoelasticity of Austenitic NiTi Shape Memory Alloys Deformed at High Strain Rate, *Mater. Sci. Eng. A*, 2021, **804**, p 140753. <https://doi.org/10.1016/j.msea.2021.140753>
4. T. Omori, Y. Sutou, R. Kainuma, and K. Ishida, Development of Cu–Al–Mn–Based Shape Memory Alloys, *Copper*, 2007 <https://doi.org/10.1002/9783527610327.CH24>
5. R. Kainuma, S. Takahashi, and K. Ishida, Ductile Shape Memory Alloys of the Cu–Al–Mn System, *J. Phys. IV*, 1995, **05**(C8), p C8-961. <https://doi.org/10.1051/JP4/199558961>
6. T. Gustmann, A. Neves, U. Kühn, P. Gargarella, C.S. Kiminami, C. Bolfarini, J. Eckert, and S. Pauly, Influence of Processing Parameters on the Fabrication of a Cu–Al–Ni–Mn Shape-Memory Alloy by Selective Laser Melting, *Addit. Manuf.*, 2016, **11**, p 23–31. <https://doi.org/10.1016/j.addma.2016.04.003>
7. A. Sato, E. Chishima, K. Soma, and T. Mori, Shape Memory Effect in $\gamma \rightleftharpoons \epsilon$ Transformation in Fe-30Mn-1Si Alloy Single Crystals, *Acta Metall.*, 1982, **30**(6), p 1177–1183.
8. A. Sato, Y. Yamaji, and T. Mori, Physical Properties Controlling Shape Memory Effect in FeMnSi Alloys, *Acta Metall.*, 1986, **34**(2), p 287–294.
9. M. Murakami, H. Yamada, T. Maruyama, and H. Tanahashi, Effects of Alloying Additions on Fe–Mn–Si Shape Memory Alloys, *ISIJ Int.*, 1990, **30**(8), p 674–679.
10. C. Czaderski, M. Shahverdi, R. Brönnimann, C. Leinenbach, and M. Motavalli, Feasibility of Iron-Based Shape Memory Alloy Strips for Prestressed Strengthening of Concrete Structures, *Constr. Build. Mater.*, 2014, **56**, p 94–105.
11. W.J. Lee, B. Weber, G. Feltrin, C. Czaderski, M. Motavalli, and C. Leinenbach, Stress Recovery Behaviour of an Fe–Mn–Si–Cr–Ni–VC Shape Memory Alloy used for Prestressing, *Smart Mater. Struct.*, 2013, **22**(12), p 125037.
12. M.R. Izadi, E. Ghafoori, M. Shahverdi, M. Motavalli, and S. Maalek, Development of an Iron-Based Shape Memory Alloy (Fe-SMA) Strengthening System for Steel Plates, *Eng. Struct.*, 2018, **174**(July), p 433–446. <https://doi.org/10.1016/j.engstruct.2018.07.073>
13. S. Kajiwara, D. Liu, T. Kikuchi, and N. Shinya, Remarkable Improvement of Shape Memory Effect in Fe–Mn–Si Based Shape Memory Alloys by Producing NbC Precipitates, *Scr. Mater.*, 2001, **44**(12), p 2809–2814.
14. C. Leinenbach, H. Kramer, C. Bernhard, and D. Eifler, Thermo-Mechanical Properties of an Fe–Mn–Si–Cr–Ni–VC Shape Memory Alloy with Low Transformation Temperature, *Adv. Eng. Mater.*, 2012, **14**(1–2), p 62–67.
15. D. Kim, K. Hong, J. Lee, W. Lee, and Y. Park, Shape Recovery and Mechanical Properties Shape Memory Alloy for Linear Actuator Application, *Phys. Metals Metallogr.*, 2022, **123**(14), p 1–10.
16. N. Stanford and D.P. Dunne, Effect of NbC and TiC Precipitation on Shape Memory in an Iron-Based Alloy, *J. Mater. Sci.*, 2006, **41**(15), p 4883–4891.
17. D. Kim, C. Park, J. Lee, K. Hong, Y. Park, and W. Lee, Microstructure, Shape Memory Behavior and Mechanical Properties of Hot Rolled Fe-17Mn-5Si-5Cr-4Ni-0.3C-1Ti Shape Memory Alloy, *Eng. Struct.*, 2021, **239**, p 112300. <https://doi.org/10.1016/j.engstruct.2021.112300>
18. “Test Pieces for Tensile Test for Metallic Materials,” KS B0801, Korean Standards Association, 2007
19. G. Wang, H. Peng, C. Zhang, S. Wang, and Y. Wen, Relationship among Grain Size, Annealing Twins and Shape Memory Effect in Fe–Mn–Si Based Shape Memory Alloys, *Smart Mater. Struct.*, 2016, **25**(7), p 075013.
20. S. Majajan, C.S. Pande, M.A. Imam, and B.B. Rath, Formation of Annealing Twins, *Acta Mater.*, 1997, **45**(6), p 2633–2638.
21. N. Stanford and D.P. Dunne, Martensite/Particle Interactions and the Shape Memory Effect in an Fe–Mn–Si–Based Alloy, *J. Mater. Sci.*, 2007, **42**(12), p 4334–4343.
22. Z. Dong, U.E. Klotz, C. Leinenbach, A. Bergamini, C. Czaderski, and M. Motavalli, A Novel Fe–Mn–Si Shape Memory Alloy with Improved Shape Recovery Properties by VC Precipitation, *Adv. Eng. Mater.*, 2009, **11**(1–2), p 40–44.
23. H.S. Yang, J.H. Jang, H.K.D.H. Bhadeshia, and D.W. Suh, Critical Assessment: Martensite-Start Temperature for the $\gamma \rightarrow \epsilon$ Transformation, *Calphad Comput. Coupling Phase Diagr. Thermochem.*, 2012, **36**, p 16–22. <https://doi.org/10.1016/j.calphad.2011.10.008>
24. J. Chen, H.B. Peng, Q. Yang, S.L. Wang, F. Song, and Y.H. Wen, Effect of Carbon Content on Shape Memory Effect of Fe–Mn–Si–Cr–Ni–Based Alloys at Different Deformation Temperatures, *Mater. Sci. Eng. A*, 2016, **677**, p 133–139.
25. L.M. Guerrero, P. La Roca, F. Malamud, A. Baruj, and M. Sade, A Short Review on the Effect of Cr on the Fcc-Hcp Phase Transition in Fe–Mn–Based Alloys, *Shape Mem. Superelasticity*, 2020, **6**(2), p 202–212. <https://doi.org/10.1007/s40830-020-00285-z>
26. P. Sahu, A.S. Hamada, R.N. Ghosh, and L.P. Karjalainen, X-Ray Diffraction Study on Cooling-Rate-Induced $\Gamma_{\text{fcc}} \rightarrow \text{Ehcp}$ Martensitic Transformation in Cast-Homogenized Fe-26Mn-0.14C Austenitic Steel, *Metall. Mater. Trans. A Phys. Metall. Mater. Sci.*, 2007, **38**(9), p 1991–2000.
27. J.-S. Hong and Y.-K. Lee, The Mechanism of Dislocation Multiplication during Thermally Induced $\gamma \leftrightarrow \epsilon$ Transformations in the Fe-17Mn Alloy, *Scr. Mater.*, 2023, **225**, p 115157. <https://doi.org/10.1016/j.scriptamat.2022.115157>
28. Y. Yang, A. Arabi-Hashemi, C. Leinenbach, and M. Shahverdi, Influence of Thermal Treatment Conditions on Recovery Stress Formation in an FeMnSi-SMA, *Mater. Sci. Eng. A*, 2021, **802**, p 140694. <https://doi.org/10.1016/j.msea.2020.140694>
29. G. Liu, Y. Liu, Y. Cheng, J. Li, and Y. Jiang, The Intergranular Corrosion Susceptibility of Metastable Austenitic Cr–Mn–Ni–N–Cu High-Strength Stainless Steel under Various Heat Treatments, *Materials*, 2019, **12**(9), p 1385.
30. X. Huang, D. Wang, and Y. Yang, Effect of Precipitation on Intergranular Corrosion Resistance of 430 Ferritic Stainless Steel, *J. Iron Steel Res. Int.*, 2015, **22**(11), p 1062–1068. [https://doi.org/10.1016/S1006-706X\(15\)30113-8](https://doi.org/10.1016/S1006-706X(15)30113-8)
31. N. Cautaerts, R. Delville, E. Stergar, J. Pakarinen, M. Verwerft, Y. Yang, C. Hofer, R. Schnitzer, S. Lamm, P. Felfér, and D. Schryvers, The Role of Ti and TiC Nanoprecipitates in Radiation Resistant Austenitic Steel: A Nanoscale Study, *Acta Mater.*, 2020, **197**, p 184–197.
32. Y. Kobayashi, J. Takahashi, and K. Kawakami, Experimental Evaluation of the Particle Size Dependence of the Dislocation-Particle Interaction Force in TiC-Precipitation-Strengthened Steel, *Scr. Mater.*, 2012, **67**(10), p 854–857. <https://doi.org/10.1016/j.scriptamat.2012.08.005>
33. Y. Jiang, Q. Gao, H. Zhang, X. Zhang, H. Li, Z. Liu, and C. Liu, The Effect of Isothermal Aging on Microstructure and Mechanical Behavior of Modified 2.5Al Alumina-Forming Austenitic Steel, *Mater. Sci. Eng. A*, 2019, **748**, p 161–172. <https://doi.org/10.1016/j.msea.2019.01.087>
34. M.J. Lai, Y.J. Li, L. Lillpopp, D. Ponge, S. Will, and D. Raabe, On the Origin of the Improvement of Shape Memory Effect by Precipitating

VC in Fe-Mn-Si-Based Shape Memory Alloys, *Acta Mater.*, 2018, **155**, p 222–235.

35. D.A. Porter, K.E. Easterling, and M.Y. Sherif, Phase transformation in metals and alloys, *Phase transformation in metals and alloys*, 3rd ed. Taylor & Francis Group, New York, 2009

Publisher's Note Springer Nature remains neutral with regard to jurisdictional claims in published maps and institutional affiliations.

Springer Nature or its licensor (e.g. a society or other partner) holds exclusive rights to this article under a publishing agreement with the author(s) or other rightsholder(s); author self-archiving of the accepted manuscript version of this article is solely governed by the terms of such publishing agreement and applicable law.